Measuring the scattering coefficient of turbid media from two-photon microscopy

David Sevrain, Matthieu Dubreuil, Aymeric Leray, Christophe Odin, Yann Le Grand

Measuring the scattering coefficient of turbid media from two-photon microscopy

David Sevrain,[1] Matthieu Dubreuil,[1] Aymeric Leray, [2] Christophe Odin,[3] and Yann Le Grand[1,*]

[1] *Université de Brest, EA 938 Laboratoire de Spectrométrie et Optique Laser (LSOL), SFR ScInBioS, 29238 Brest Cedex 3, France*
[2] *Université de Lille-Nord de France, USR CNRS 3078 Institut de Recherche Interdisciplinaire (IRI), 59650 Villeneuve d'Ascq, France*
[3] *Université de Rennes 1, UR1/UMR CNRS 6251 Institut de Physique de Rennes (IPR), 35042 Rennes Cedex France*
[*]*yann.legrand@univ-brest.fr*

Abstract: In this paper, we propose a new and simple method based on two-photon excitation fluorescence (TPEF) microscopy to measure the scattering coefficient μ_s of thick turbid media. We show, from Monte Carlo simulations, that μ_s can be derived from the axial profile of the ratio of the TPEF signals epi-collected by the confocal and the non-descanned ports of a scanning microscope, independently of the anisotropy factor g and of the absorption coefficient μ_a of the medium. The method is validated experimentally on tissue-mimicking optical phantoms, and is shown to have potential for imaging the scattering coefficient of heterogeneous media.

References and links

1. V. V. Tuchin, "Light scattering study of tissues," Phys.- Usp. **40**(5), 495–515 (1997).
2. V. V. Tuchin, Handbook of Biomedical Diagnostics, **PM107** (SPIE Press, 2002).
3. L.-V. Wang and H. Wu, *Biomedical Optics, Principles and Imaging* (Wiley Inter-Science 2007).
4. S. L. Jacques, B. Wang, and R. Samatham, "Reflectance confocal microscopy of optical phantoms," Biomed. Opt. Express **3**(6), 1162–1172 (2012).
5. W. Denk, J. H. Strickler, and W. W. Webb, "Two-photon laser scanning fluorescence microscopy," Science **248**(4951), 73–76 (1990).
6. A. Leray, C. Odin, E. Huguet, F. Amblard, and Y. Le Grand, "Spatially distributed two-photon excitation fluorescence in scattering media: Experiments and time-resolved Monte Carlo simulations," Opt. Commun. **272**(1), 269–278 (2007).
7. Y. Le Grand, A. Leray, T. Guilbert, and C. Odin, "Non-descanned versus descanned epifluorescence collection in two-photon microscopy: Experiments and Monte Carlo simulations," Opt. Commun. **281**(21), 5480–5486 (2008).
8. E. Beaurepaire and J. Mertz, "Epifluorescence collection in two-photon microscopy," Appl. Opt. **41**(25), 5376–5382 (2002).
9. H. Szmacinski, I. Gryczynski, and J. R. Lakowicz, "Spatially localized ballistic two-photon excitation in scattering media," Biospectroscopy **4**(5), 303–310 (1998).
10. A. Leray, C. Odin, and Y. Le Grand, "Out-of-focus fluorescence collection in two-photon microscopy of scattering media," Opt. Commun. **281**(24), 6139–6144 (2008).
11. S. L. Jacques, "Light distributions from point, line and plane sources for photochemical reactions and fluorescence in turbid biological tissues," Photochem. Photobiol. **67**(1), 23–32 (1998).
12. W. R. Zipfel, R. M. Williams, and W. W. Webb, "Nonlinear magic: multiphoton microscopy in the biosciences," Nat. Biotechnol. **21**(11), 1369–1377 (2003).
13. G. Marsaglia and T. A. Bray, "A Convenient Method for Generating Normal Variables," SIAM Rev. **6**(3), 260–264 (1964).
14. N. Ghosh, H. S. Patel, and P. K. Gupta, "Depolarization of light in tissue phantoms - effect of a distribution in the size of scatterers," Opt. Express **11**(18), 2198–2205 (2003).
15. L. G. Henyey and J. L. Greenstein, "Diffuse radiation in the galaxy," Astrophys. J. **93**, 70–83 (1941).
16. C. Xu, R. M. Williams, W. Zipfel, and W. W. Webb, "Multiphoton excitation cross-sections of molecular fluorophores," Bioimaging **4**(3), 198–207 (1996).

17. M. Daimon and A. Masumura, "Measurement of the refractive index of distilled water from the near-infrared region to the ultraviolet region," Appl. Opt. **46**(18), 3811–3820 (2007).
18. A. Jain, A. H. J. Yang, and D. Erickson, "Gel-based optical waveguides with live cell encapsulation and integrated microfluidics," Opt. Lett. **37**(9), 1472–1474 (2012).
19. S. N. Kasarova, N. G. Sultanova, C. D. Ivanov, and I. D. Nikolov, "Analysis of the dispersion of optical plastic materials," Opt. Mater. **29**(11), 1481–1490 (2007).
20. W.-F. Cheong, S. A. Prahl, and A. J. Welch, "A review of the optical properties of biological tissues," IEEE J. Quantum Electron. **26**(12), 2166–2185 (1990).

1. Introduction

Non-invasive measurement of the optical properties of tissues offers interesting possibilities and perspectives in terms of *in vivo* diagnosis and therapy [1]. For this purpose, the so-called therapeutic window (wavelength range comprised between 0.6 and 1.3μm) is generally used to both prevent photodamage and increase penetration depth [2]. As scattering prevails over absorption within this wavelength range, tissues then behave mainly like turbid media. By excluding interfacial, inhomogeneity and polarization effects, such media can be characterized by three optical parameters which are the scattering coefficient μ_s (the inverse of the mean free path l_s between two scattering events), the associated anisotropy factor $g = <\cos\theta>$ (the average cosine of the scattering angle θ) and the absorption coefficient μ_a ($\mu_a <<$ μ_s in the relevant wavelength range). Generally, measurement of these parameters *in vivo* or simply within thick samples rules out transmission geometries. Moreover the usual backscattering methods based on the diffusion theory like diffuse reflectance provide a reduced scattering coefficient $\mu'_s = \mu_s(1-g)$ but fail to separate μ_s and g ([3] and references therein). In order to measure μ_s independently of g within thick samples, it is necessary to consider backward layouts able to select unscattered or ballistic photons to the detriment of scattered ones. In that case, μ_s can be derived from an apparent attenuation coefficient obtained by fitting the measured intensity as a function of depth with a Beer-Lambert law. Reflectance confocal laser microscopy has been recently shown to have potential to measure μ_s by isolating unscattered light produced by backscattering of a focusing laser beam within the focal volume of an objective lens [4]. However, evaluation of μ_s from the measured axial profile of the backscattered intensity detected through a confocal pinhole is highly model-dependent. Indeed, as a high-NA objective lens is used to localize the backscattering source, the extra-path length of photons has to be considered. Modeling the scattering coefficient as a function of the apparent attenuation coefficient then lays on the calculation of a geometrical correcting factor which depends on the expected angular dependence of both excitation and backscattered light. Furthermore, an additional correction depending on the value of g is necessary; it is obtained empirically using Monte Carlo simulations in order to account for the contribution of the laser photons reaching the focus despite scattering. Finally, the authors have neglected the effect of absorption although the measured attenuation coefficient is modified by both absorption and scattering.

In this paper we propose a new and simple method able to measure μ_s independently of g and μ_a within thick turbid media. It is based on two-photon microscopy and circumvents the drawbacks of the reflectance confocal microscopy method listed above. Indeed, by measuring the axial profile of the ratio of the collection efficiencies detected by the confocal and non-descanned ports of a two-photon fluorescence scanning microscope, we demonstrate the possibility of measuring an apparent scattering coefficient, independently of μ_a, g, and of the microscope excitation function. Moreover, a simple analytical model was developed for recovering with a very good accuracy the true scattering coefficient from the apparent one.

The paper is organized as follows. In Section 2, we present in detail the principle of our method. Then, the results of Monte Carlo simulations of the collection efficiency performed in order to validate our concept are reported in section 3. In section 4, we describe a simple analytical model valid for high-NA objectives, which makes it possible to get back to the true scattering coefficient. Finally, we present in section 5 experimental results from various

scattering biomimetic media made of polystyrene spheres embedded in agarose gel matrices. We show the ability of our technique for discriminating between two different scattering media either superposed or side-by-side.

2. Principle of the method

Two-photon excitation fluorescence (TPEF) microscopy takes advantage of the intrinsic localization of nonlinear absorption within the focal volume of the objective lens to image beyond the mean free path $l_s = \mu_s^{-1}$ of turbid media [5,6]. Robustness to scattering results mainly from the ability to avoid descanned (DS) collection modalities used in confocal microscopy. Indeed, even after removal of the confocal pinhole, DS paths have still low fields of view (FOV) which are inconsistent with efficient collection of scattered light. Wide FOV non-descanned (NDS) pathways are then preferred in TPEF microscopy; they consist in directly reimaging the rear pupil of the objective lens onto an external detector which is set as close as possible to the collecting optics [7,8]. The effective FOV of well-designed NDS setup is then just limited to that of the objective itself. Moreover, by remarking that tissues have generally high g-values (g>0.8) and using a long working distance objective, the NDS collection efficiency η_{NDS} was shown to remain almost constant up to an imaging depth z_0 approximately equal to the radius r_{fov} of the collecting FOV of the microscope [7,8]. This depth range where η_{NDS} is almost constant is equal to a few hundreds of microns for high-NA objective lenses used in two-photon microscopy. On the contrary, if absorption is neglected, the collection efficiency η_{conf} of the confocal path decreases exponentially with z_0, like the probability for a fluorescence photon not to be scattered before exiting the turbid medium, expressed by $\exp(-\mu_s^{app} z_0)$. Here μ_s^{app} corresponds to an apparent scattering coefficient. Due to the isotropic fluorescence emission, μ_s^{app} can be easily related to the true coefficient μ_s, independently of g, by averaging the Beer-Lambert law over all photon paths within the numerical aperture of the collecting objective, as shown in section 4. Unfortunately, direct measurement of η_{conf} is not possible because the detected fluorescence signal further depends on the excitation function of the microscope f_{exc}. Since TPEF intensity is mainly produced by ballistic laser photons reaching the objective focal volume [9], f_{exc} is also expected to decrease exponentially with the imaging depth z_0 as $\exp(-2\mu_s^{exc} z_0)$, where μ_s^{exc} is the scattering coefficient for the excitation wavelength. Moreover f_{exc} depends on many parameters like the average laser power $\overline{P}$, the pulse width τ, the pulse repetition rate f, the concentration of fluorophores C, the two-photon cross-section σ_{TPEF} and the quantum yield Φ of the excited fluorophores. However, the TPEF process is independent of the collection modality, whether confocal or non-descanned [10]. The collected fluorescence signal F_{coll} is then written as:

$$F_{conf}^{coll} = f_{exc}\left(\overline{P}, \tau, f, C, \sigma_{TPEF}, \Phi, \mu_s^{exc}, z_0\right)\eta_{conf} \tag{1.a}$$

for the confocal pathway, and:

$$F_{NDS}^{coll} = f_{exc}\left(\overline{P}, \tau, f, C, \sigma_{TPEF}, \Phi, \mu_s^{exc}, z_0\right)\eta_{NDS} \tag{1.b}$$

for the non-descanned pathway. Consequently, $F_{conf}^{coll}/F_{NDS}^{coll}$ is independent of the excitation function of the microscope, and since η_{NDS} is almost constant for shallow depths, it comes:

$$F_{conf}^{coll}/F_{NDS}^{coll} \propto \eta_{conf} \approx \exp\left(-\mu_s^{app} z_0\right) \tag{2}$$

Then measuring $F_{conf}^{coll}/F_{NDS}^{coll}$ as a function of the imaging depth z_0 provides a robust method to recover the apparent scattering coefficient, which is directly related to the true scattering coefficient. Furthermore, we show in the next section that the absorption by the sample does not contribute significantly to the decay of this ratio.

3. Monte Carlo simulations

Our Monte Carlo simulations of η_{conf} and η_{NDS} were based on a program developed for modeling photon transport in living tissues [11]. The collection efficiency of the microscope was defined as the ratio of the number of photons collected through the scattering medium with respect to the total number of photons emitted by the fluorescence source. In order to take into account diffraction in the simulation of the collection efficiency η_{conf} through a confocal pinhole with a finite size, the TPEF source was assumed to be confined in a small focal volume (centered on the geometrical focus of the objective lens) corresponding to the two-photon illumination point-spread function ($IPSF^2$) of the microscope [12]. Fluorescence photons were then launched isotropically from this volume (see Fig. 1).
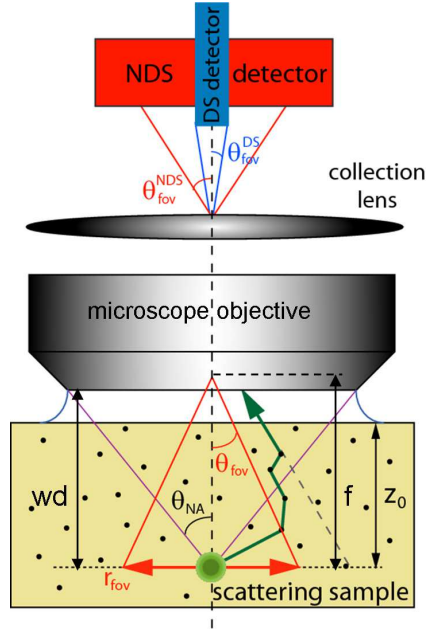

Fig. 1. Geometry of the collection paths used in the Monte Carlo simulations and useful parameters. f: focal length of the objective; wd: working distance; θ_{NA}: numerical aperture angle; r_{fov}: linear field of view; θ_{fov}^{DS} and θ_{fov}^{NDS}: angular field of view of the confocal (or descanned DS) and non-descanned NDS ports, respectively.

The starting coordinates of these photons were sampled as normal random variables using the Marsaglia polar method [13] and a Gaussian probability density determined by the diffraction-limited lateral and axial extents of the $IPSF^2$ noted respectively w_{xy} and w_z [12]. It is worthwhile to note that w_{xy} and w_z stand for the 1/e half-widths of the $IPSF^2$. To insure good statistics on the number of collected photons, especially when $\eta_{conf} \ll 1$ for imaging depths $z_0 > \mu_s^{-1}$, $N = 5.10^6$ photons were launched from each depth z_0. Photon propagation within the turbid medium consisted on simple ray-tracing based on geometrical optics, phase and polarization being insignificant in case of forward scattering of incoherent light like fluorescence in tissue-mimicking optical phantoms [14]. The step size 's' between two scattering events and the cosine of the deflection angle were sampled according to probability densities derived from respectively the Beer-Lambert law and the Henyey-Greenstein phase function [15]. Assuming a random number ξ uniformly distributed over the interval [0,1], standard sampling expressions were then $s = -\ln(\xi)/\mu_s$ and $\cos\theta = (1 + g^2-[(1-g^2)/(1-g + 2g\xi)]^2)/2g$ if $g \neq 0$ or $\cos\theta = 2\xi-1$ if $g = 0$. The scattering azimuthal angle ψ was assumed to be uniformly distributed over $[0,2\pi]$, then sampled as $\psi = 2\pi\xi$. The turbid medium was

considered homogeneous. Absorption was accounted by attributing an initial weight of 1 to each launched photon, then multiplying this weight by a factor $\mu_s/(\mu_s + \mu_a)$ for each scattering event. Since the turbid medium was first considered as semi-infinite and bounded by one exit plane, it was necessary to limit the scattering volume in order to minimize the computation time. Photons were then considered lost beyond a preset distance of typically 10 times the effective mean free path (scattering volume $\sim 1 cm^3$). The exit plane was assumed smooth for not altering photon trajectory. Index matching between the turbid sample and the immersion medium was assumed, thus Fresnel refraction and reflection at this interface were not considered. Once photons escaped from the turbid medium, conditions for epi-collection were two-fold: photons had to hit the objective's front aperture and to enter the FOV of the microscope [7]. Photon trajectories which fulfilled the first condition were retraced back to the focal plane of the objective lens. To account for diffraction at collection, a weight was assigned to each of these photons according to their position with respect to the optical axis. The weighting function was obtained numerically from the convolution of a circular aperture, corresponding to the FOV of the microscope, and a Gaussian function, representing the PSF of the objective at the collection wavelength (i.e. 600nm, see section 5 for details). Note that the FOV of the microscope is proportional to the pinhole diameter for confocal collection (see below for details).

Figure 2 is a semi-log representation of our Monte Carlo simulations of η_{conf}/η_0 and η_{NDS}/η_0 as a function of the imaging depth z_0, where $\eta_0 = (1-\cos\theta_{NA})/2$ is the collection efficiency in clear medium of the objective lens of half-angle aperture θ_{NA}. The simulated water immersion (n = 1.33) objective lens was a long working distance (wd = 2mm), NA = 0.9 (NA = n.$\sin\theta_{NA}$) and 60 × magnification model which equipped our microscope. The scattering coefficient of the turbid medium was fixed to $\mu_s = 100cm^{-1}$. Simulations were performed for two absorption coefficients $\mu_a = 0$ and $\mu_a = \mu_s/10 = 10cm^{-1}$ and two anisotropy factors g = 0.85 and 0.95. Moreover, η_{conf} was calculated for the smallest (#1) and the largest (#4) pinholes of our scanning microscope, whose diameters Φ_p are respectively of 60 and 200μm. The corresponding values of the FOV radius r_{fov} in the focal plane of the aforementioned 60 × objective lens was found to be 0.14μm for pinhole 1 and 0.47μm for pinhole 4, using the relation $r_{fov} = \Phi_p/(2 \times 3.55 \times 60)$. The factor of 3.55 in this formula stands for the ratio of the focal lengths of the pinhole focusing lens and the scan lens. Note that the r_{fov} values bound the lateral extent $w_{xy} \approx 0.21 \mu m$ of the IPSF[2] found for a 0.9-NA water-immersion objective lens at the illumination wavelength $\lambda \approx 830nm$ of our femtosecond laser. Moreover r_{fov} for the NDS collection path was previously measured to be 320μm in the focal plane of the 60 × lens [6]. This explains why the simulations were ended at a depth $z_0 = 300\mu m$. In fact, η_{NDS} is almost constant for $\mu_a = 0$ (see Fig. 2) within this depth range.
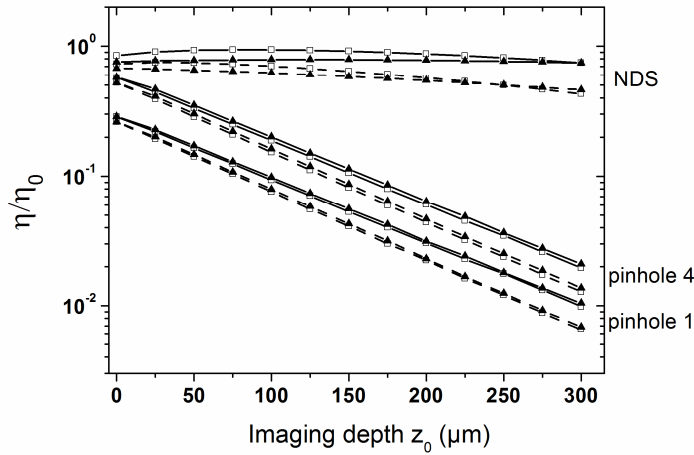
Fig. 2. Monte Carlo simulations of the z-profile of collection efficiencies η_{conf} (pinhole 1 and 4) and η_{NDS}, without absorption (full lines) and with absorption $\mu_a = 10\text{cm}^{-1}$ (dashed lines), for g = 0.85 (empty square) and g = 0.95 (full triangle). The vertical scale is logarithmic and $\mu_s = 100\text{cm}^{-1}$.

Monte Carlo simulations of the collection efficiencies through pinholes 1 and 4 (confocal paths) are well fitted with almost parallel straight lines (see Fig. 2 and correlation coefficient $R^2 > 0.999$ in Table 1), in agreement with the exponential behavior expected for the collection efficiency with confocal modality. Note that the collection efficiency for the largest confocal pinhole is higher than that for the smallest one. In fact, depending on the pinhole diameter, more or less ballistic photons from the fluorescent focal volume are collected through the confocal pathway, but not any significant scattered photons. The slopes of the curves, or the apparent scattering and attenuation coefficients, range from about 111.6 to 113.1cm^{-1} without absorption and from 122.6 to 124.2cm^{-1} with absorption, depending on the size of the pinhole and of g (see Table 1). Note that the apparent coefficient is found systematically smaller for the smaller pinhole.

Table 1. Slopes of the curves of Fig. 2 (in cm^{-1}). The correlation coefficient R^2 of the linear fit is shown in brackets. For pinholes 1 and 4, these values represent the apparent scattering coefficient μ_s^{app} (or attenuation coefficient in the case of absorption), obtained directly from the collection efficiency η.

| | $\mu_s = 100\text{cm}^{-1}$, $\mu_a = 0$ | | $\mu_s = 100\text{cm}^{-1}$, $\mu_a = 10\text{cm}^{-1}$ | |
	g = 0.85	g = 0.95	g = 0.85	g = 0.95
Pinhole 1	112.4 (0.9999)	111.6 (0.9998)	123.3 (0.9999)	122.6 (0.9999)
Pinhole 4	113.1 (0.9999)	112.0 (0.9997)	124.2 (0.9999)	122.9 (0.9998)
NDS	5.7 (0.524)	0.7 (0.153)	19.0 (0.934)	13.0 (0.984)

This can be explained by the fact that when the pinhole diameter decreases, there is a decrease of the collection efficiency for the off-axis ballistic fluorescence photons originating from the PSF but outside the geometrical focal plane, although these photons strike the objective's front aperture. This effect promotes the collection of paraxial photons with shortest path lengths near to the imaging depth z_0, and then reduces the apparent attenuation coefficient. We then expect that the value of the apparent scattering coefficient found from our Monte Carlo simulations for the largest confocal pinhole ($\mu_s^{app} = 113.1\text{cm}^{-1}$) will be closer to that obtained from a simple analytical model considering collection of the ballistic

photons only (see next section). It is also worthwhile to note that for confocal modality, similar results of the apparent scattering coefficient were obtained for different g within the range [0.80-0.98]. However, for g<0.8, the axial profile of the NDS collection efficiency is not flat enough for considering η_{NDS} as constant within this relevant depth range. Moreover, for g≥0.99 (peaked forward scattering), some scattered photons are not enough deflected to be rejected by the confocal pinhole. In that case, the apparent scattering coefficient decreases and its value depends on both values of g and Φ_p.

In order to assess the validity of the method, we have calculated the confocal to non-descanned ratios. For the sake of clarity, we have only presented in Fig. 3 the ratios η_{conf}/η_{NDS} for pinhole 4, which is the pinhole used for the experiments (section 5).
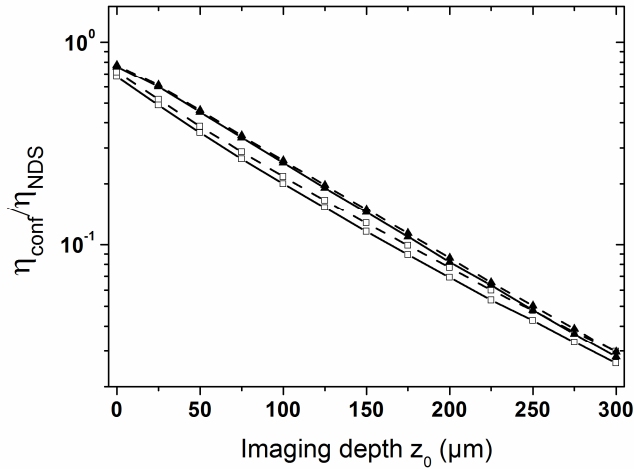

Fig. 3. Monte Carlo simulations of the z-profile of collection efficiencies ratio η_{conf}/η_{NDS} for pinhole 4, without absorption (full lines) and with absorption $\mu_a = 10cm^{-1}$ (dashed lines), for g = 0.85 (empty square) and g = 0.95 (full triangle). The vertical scale is logarithmic.

Simulations demonstrate that the ratio is almost independent of μ_a and g. Indeed, the slopes of the fitted curves, i.e. values of the apparent scattering coefficient, do not vary from more than 5% whatever the values of μ_a and g (see Table 2).

Table 2. Slopes of the curves of Fig. 3. The correlation coefficient R^2 of the linear fit is shown in brackets. These values represent the apparent scattering coefficient μ_s^{app}, obtained from the collection efficiency ratio η_{conf}/η_{NDS}, for pinhole 4.

	$\mu_s = 100cm^{-1}, \mu_a = 0$		$\mu_s = 100cm^{-1}, \mu_a = 10cm^{-1}$	
	g = 0.85	g = 0.95	g = 0.85	g = 0.95
μ_s^{app} (cm^{-1})	107.5 (0.9977)	111.2 (0.9998)	105.2 (0.9978)	109.9 (0.9998)

4. Apparent scattering coefficient

In this section, we introduce a simple model to derive the true scattering coefficient μ_s from the measured apparent one μ_s^{app}. In this simple model, we assumed that only ballistic photons emitted from the geometrical focus at depth z_0 beneath the scattering sample surface are epi-collected by the objective lens. The detected intensity $I(z_0,\mu_s)$ was then calculated by averaging the unscattered intensity transmitted by the medium over the solid angle of the collecting objective. I_0 being the overall fluorescence intensity emitted over 4π sr from the geometrical focus, the collection efficiency for the ballistic intensity can be written as:

$$\eta_{bal}\left(z_0,\mu_s\right) = \frac{I\left(z_0,\mu_s\right)}{I_0} = \frac{1}{2}\int_1^{CA^{-1}}\frac{\exp\left(-\mu_s z_0 u\right)}{u^2}du \qquad (3)$$

where u = 1/cosθ and CA = cosθ_NA. The factor exp(-μ_sz_0/cosθ) in Eq. (3) is the probability for a photon not to be scattered when it propagates through the turbid medium with an angle θ from the optical axis. When μ_sz_0 → 0, η_bal reduces to η_0 = (1-cosθ_NA)/2, which corresponds to the collection efficiency either without scattering (μ_s→ 0) or at zero depth (z_0→ 0).

Since Monte Carlo simulations showed that the collection efficiency in the confocal mode scales like exp(-μ_s^app z_0), we performed a numerical integration of Eq. (3) over the aperture of the objective lens used in our experiments (0.9-NA water immersion objective, CA = cos[arcsin(NA/n)] = 0.7363), for different products μ_sz_0. The results are represented as a function of z_0 in Fig. 4(a), for various μ_s. Data points are well fitted by first order polynomials for imaging depths z_0 comprised in the interval [0-300μm], and μ_s varying from 10 to 250cm^{-1} (correlation coefficient R^2 > 0.9999). The slopes of the fits provide an apparent scattering coefficient μ_s^app which is represented as a function of μ_s in Fig. 4(b). As expected, we find μ_s^app > μ_s, since all the photon paths are either larger or equal to z_0. In addition, the difference between μ_s^app and μ_s increases as μ_s increases. Note that when μ_s≈100cm^{-1} the curve of Fig. 4(b) provides μ_s^app ≈114.5cm^{-1}, which is in good agreement with the value obtained from Monte Carlo simulation, especially for the largest confocal pinhole (μ_s^app ≈113.1cm^{-1} for g = 0.95, see Table 1).
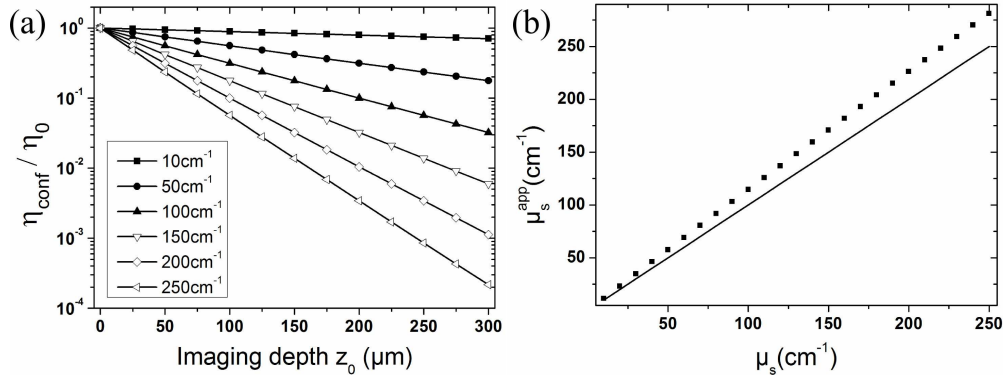

Fig. 4. (a) Epi-collection efficiencies for the ballistic fluorescence photons produced by two-photon excitation at focus of a water immersion objective with NA = 0.9, as a function of the imaging depth z_0 in a turbid medium with various scattering coefficients. Dots were obtained from numerical integration of Eq. (3) whereas full lines are the corresponding linear regressions. (b) apparent scattering coefficient μ_s^app derived from curve fitting of Fig. 4(a) as function of the true scattering coefficient μ_s. The full line is a guide for the eye (bisector).

Moreover using Taylor-series developments and least squares methods, we found that μ_s can be well approximated from μ_s^app using the following relationship:

$$\mu_s^{corr} = \frac{2A\mu_s^{app}}{1+\sqrt{1-2\mu_s^{app}z_{corr}B}} \qquad (4)$$

where A = [CA-1]/lnCA, B = [A^2/CA]-1, z_{corr} = [$<z_0^3>$-$<z_0><z_0^2>$]/[$<z_0^2>$-$<z_0>^2$] with $<z_0^n>$ = $\sum_p<z_{0p}^n>$/N, where N is the number of depth values z_{0p} which are considered for fitting the data (from 0 to 300μm by 25μm step). Here, μ_s^{corr} stands for the corrected scattering coefficient, calculated from Eq. (4). For the objective lens and axial steps used in our experiment, we obtained A≈0.8614, B≈7.836.10^{-3}, and z_{corr} = 300μm. Using these parameters in Eq. (4), we recovered μ_s^{corr}≈100cm^{-1} from the previous value μ_s^app≈114.5cm^{-1}. It is

worthwhile to note that because $B \ll 1$, $\mu_s^{corr} \approx A.\mu_s^{app}$ for small depths z_0 of the order of $1/\mu_s$. Note that this simplified expression can be easily recovered by considering a first-order development of $\exp(-\mu_s z_0 u)$ in Eq. (3). The corrected scattering coefficients μ_s^{corr} recalculated from Eq. (4) are plotted as a function of the starting values of μ_s in Fig. 5(a). As can be seen, the recalculated points almost superimpose the bisector. The relative error is plotted in Fig. 5(b), indicating a good agreement with discrepancies of the order of 0.3% for μ_s as large as 250cm^{-1}.
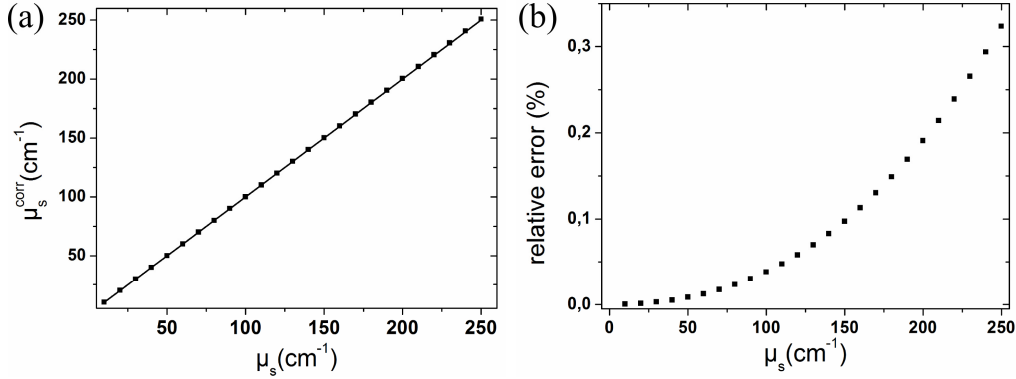

Fig. 5. (a) Corrected scattering coefficient μ_s^{corr} from Eq. (4) versus true scattering coefficient μ_s ; (b) Relative error between μ_s^{corr} and μ_s.

Table 3 shows the corrected scattering coefficients derived from the apparent ones obtained from Monte Carlo simulations for a scattering medium with $\mu_s = 100 \text{cm}^{-1}$.

Table 3. Corrected scattering coefficient μ_s^{corr} from the apparent scattering coefficients μ_s^{app} obtained from Monte Carlo simulations for a scattering medium with $\mu_s = 100\text{cm}^{-1}$ (see Table 2).

	$\mu_a = 0$		$\mu_a = 10\text{cm}^{-1}$	
	g = 0.85	g = 0.95	g = 0.85	g = 0.95
μ_s^{corr} (cm^{-1})	93.8	97.1	91.8	95.9

Thus for a limited range of imaging depths and with well-known and well-chosen objective parameters, measuring the confocal-to-NDS fluorescence intensity ratio on a two-photon microscope enables to retrieve the true scattering coefficient of a turbid medium, with accuracy better than 10%, almost independently of the anisotropy factor, the absorption coefficient or the size of the confocal pinhole (comparing values of μ_s^{app} in Table 1 for pinholes 1 and 4).

5. Materials

5.1 Two-photon microscope

A two-photon excitation fluorescence microscope based on an infrared (IR) coated confocal microscope (FV300/BX51WI, Olympus France, Rungis) and a femtosecond Ti:Sapphire laser (Verdi-V5/Mira, Coherent France, les Ulis) tuned at $\lambda = 830\text{nm}$ were used in this study (pulse duration ~200fs). A home-built NDS port was mounted abreast of the fluorescence cube turret, on the left side of the microscope, in association with a home-built cube containing a dichroic mirror (675DCXRU, Chroma, Brattleboro, USA) and a high aperture collection lens [6]. The external photomultiplier tube (PMT) module (H7710-13, Hamamatsu Photonics France, Massy) of the NDS port was connected to a transimpedance amplifier (C7319,

Hamamatsu Photonics France, Massy) in order to fit the internal PMT of the DS port and use the full range of the electronics and software of the confocal microscope. IR blocking filters (Schott BG39 model, Edmund Optics Europe, York, UK) were inserted on both the DS and NDS pathways. A long working distance objective lens (LUMPlanFl 60 × /0.90W, Olympus France, Rungis) was water-coupled to the phantoms.

5.2 Optical phantoms

Experiments were carried out on tissue mimicking scattering phantoms based on polystyrene microspheres in aqueous agarose gels. More precisely polystyrene microspheres (Polysciences Inc., USA) of various diameters were embedded in a 4% agarose gel matrix (Sigma-Aldrich Co., USA). In order to produce two-photon excitation fluorescence, a water-diluted solution of sulforhodamine B (Kiton Red 620®, Exciton, USA) was added to the gel at a final concentration of about 20µM. Laser excitation wavelength was set at 830nm to fit with the maximum of two-photon cross-section of Kiton Red 620® [16]. The maximum of the fluorescence spectrum measured from the labelled gels was obtained for a wavelength λ_{max} of ~600nm (FWMH~30nm). This value was then applied as the collection wavelength in all our simulations and measurements. The emission peak was assumed narrow enough (FWMH/λ_{max}~5%) to consider $\mu_s(\lambda_{max})$ and the inherently wavelength-averaged experimental μ_s in good agreement. The refractive indices of agarose gels n_a and polystyrene spheres n_s for this wavelength were respectively fixed to $n_a \approx n_{water} = 1.33$ [17,18] and $n_s = 1.59$ [19]. Bead concentrations were calculated from Wu and Wang's code [3] based on Mie theory in order to obtain scattering coefficients of 50cm^{-1} and 100cm^{-1} at 600nm. Bead diameters of 0.54µm, 1.53µm and 4.52µm were selected for this study, resulting in anisotropy factors g of respectively 0.85, 0.93 and 0.87 which are typical of biological tissues in which forward scattering prevails [20]. Table 4 summarizes the properties of the tissue phantoms.

Table 4. Microsphere diameters and concentrations, and resulting scattering properties of agarose gels used as tissue-mimicking samples. Error bars were estimated from the uncertainty on volumes taken from stock solutions of microbeads.

Bead diameter (µm)	Anisotropy factor g	Concentration (beads.cm^{-3})	Scattering coefficient at λ = 600nm (cm^{-1})
0.54	0.85	$(5.4 \pm 0.3) \times 10^{10}$	100.0 ± 6.5
		$(2.7 \pm 0.2) \times 10^{10}$	50.0 ± 3.4
1.53	0.93	$(1.5 \pm 0.1) \times 10^{9}$	100.0 ± 6.7
		$(7.6 \pm 0.4) \times 10^{8}$	50.0 ± 2.4
4.52	0.87	$(2.4 \pm 0.1) \times 10^{8}$	100.0 ± 6.1
		$(1.2 \pm 0.8) \times 10^{8}$	50.0 ± 3.2

Custom ~1cm^3-cylindrical wells were drilled in a PMMA plate and coverslips were glued on the top to obtain an optical quality interface. Before polymerization of agarose, the mixtures were injected within the wells through small ducts drilled on the bottom of the plate, then sealed to prevent evaporation. The mixtures were further used to load rectangle glass capillaries of inner thickness from 100 to 600µm with a step size of 100µm (CM Scientific Ltd., Silsden, UK). These allowed us to evaluate independently the scattering coefficients from a simple collimated transmission experiment [3]. Abreast and superposed gels of distinct scattering coefficients were also prepared to determine if our technique was able to reveal lateral and axial (in-depth) heterogeneities of the scattering coefficient.

6. Experimental results

As previously explained, our method is based on the measurement of the confocal-to-NDS fluorescence intensity ratios of a two-photon microscope as a function of imaging depth. In order to optimize the signal-to-noise ratio while avoiding photobleaching, intensity measurements were averaged on a small area of the gels rather than at fixed points. Z-stacks

of zoomed images were then acquired over a depth range for which the NDS collection efficiency of the microscope can be considered constant (i.e. 320μm, corresponding to the field of view of the NDS port). Zooming allowed reduction of the scan angle which provides experimental conditions close to those of the simulations where the fluorescence source was considered on the optical axis. To further improve the signal-to-noise ratio, images were averaged over two scans using Kalman filtering. Laser power at the objective was determined at the beginning of the experiment for maximizing TPEF intensity near the sample surface while avoiding photobleaching. The PMT supplied voltages were also set at first to exploit the full 12-bit intensity resolution of the microscope.

The six wells filled with the scattering gels prepared as described above were imaged from the surface to the bottom with an axial step size of 10μm. Imaging was performed successively through the DS port (confocal) equipped with the pinhole 4 (diameter 200μm) and the NDS port. The overall acquisition time of a complete image stack was less than one minute. For gels with scattering coefficient of $100cm^{-1}$, the signal-to-noise ratio was not high enough with confocal modality to obtain reliable measurements beyond a depth of about 200μm. The mean intensity value of the 256×256 pixels^2 images after background subtraction was calculated using ImageJ (NIH freeware, Measure Stacks plugin) and considered as a measure of the TPEF signal. Figure 6 is a semi-log representation of the measured confocal-to-NDS intensity ratios as a function of depth for the six wells. Linear fitting of the experimental data (straight lines), excluding the first 30μm close to the sample surface for which measurements were not reliable, provides the actual scattering coefficient from the apparent one according to the model of section 4. The collimated transmission method was implemented in parallel on a series of 100 to 600μm-thick capillaries loaded with the same scattering gels, using a 633nm He-Ne laser as a source. A series of capillaries loaded with clear fluorescent gels was used as reference to correct measurements for residual optical losses due to absorption of the dye and Fresnel reflections. The results are summarized in Table 5. Although some differences with anticipated values exist, the scattering coefficients derived from the two methods are in excellent agreement if one takes into account measurement uncertainties. Moreover, as expected, the results appear independent of the anisotropy factor g (0.85 to 0.93 see Table 4). This clearly demonstrates the relevance of our new approach.
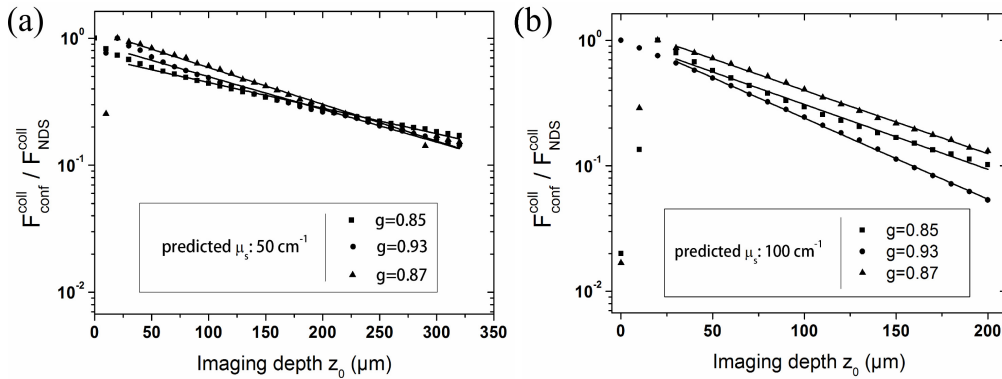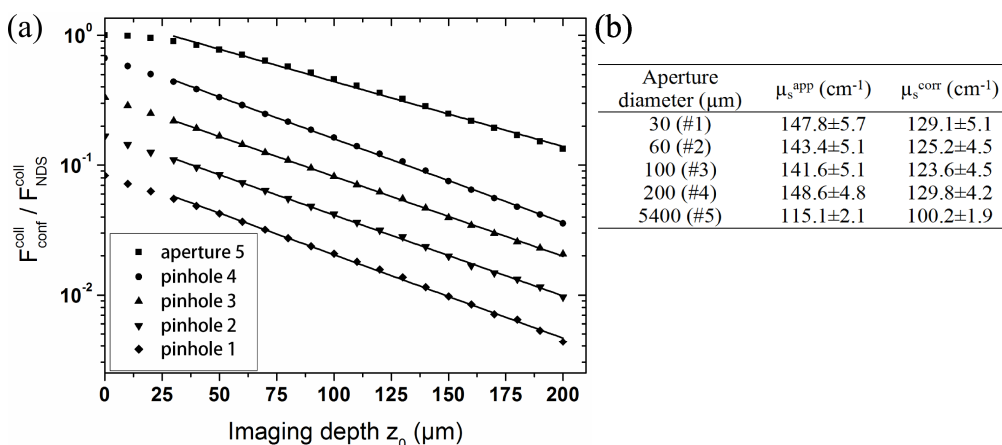

Fig. 6. Semi-log representation of the confocal-to-nondescanned ratios of the two-photon excitation fluorescence intensity versus imaging depth measured from six scattering gels with scattering coefficients of ~50cm^{-1} and ~100cm^{-1}, and three distinct anisotropy factors (see Table 4). The confocal pinhole has a diameter of 200μm (pinhole 4). Straight lines stand for linear fits of experimental data (dots), allowing to determine the true scattering coefficients through Eq. (4).

Table 5. Scattering coefficients of agarose gel mixtures for three bead diameters, i.e. three different anisotropy factors g. The scattering coefficients are from left to right: the scattering coefficient anticipated from Mie theory (μ_s^{ant}), the apparent coefficient derived from the confocal-to-NDS ratio (μ_s^{app}), the corresponding scattering coefficient as obtained after correction (μ_s^{corr}) and the ones obtained from the collimated transmission method (μ_s^{trans}). Errors bars on the experimental scattering coefficients were obtained from statistics on two-photon images and from repetitive measurements for the collimated method.

Beads diameter (μm)	Anisotropy factor g	μ_s^{ant} (cm^{-1})	μ_s^{app} (cm^{-1})	μ_s^{corr} (cm^{-1})	μ_s^{trans} (cm^{-1})
0.54	0.85	50.0 ± 3.4	46.4 ± 3.5	40.2 ± 3.0	40.2 ± 2.9
		100.0 ± 6.5	119.1 ± 2.0	103.7 ± 1.8	99.8 ± 4.3
1.53	0.93	50.0 ± 2.4	59.3 ± 1.4	51.5 ± 1.2	51.7 ± 4.1
		100.0 ± 6.7	148.6 ± 4.8	129.8 ± 4.2	131.7 ± 6.1
4.52	0.87	50.0 ± 3.2	66.6 ± 3.5	57.9 ± 3.1	59.9 ± 2.8
		100.0 ± 6.1	116.2 ± 7.3	101.2 ± 6.5	105.6 ± 5.4

We have also evaluated the robustness of our method with respect to the size of the pinhole. The confocal-to-NDS ratio measured as a function of the imaging depth for the four confocal pinholes and a fifth aperture, much larger than the others, are represented in Fig. 7. Note that this aperture was obtained by removing the fifth pinhole of the confocal wheel so as to allow two-photon imaging modality via the DS port.

(b)

Aperture diameter (μm)	μ_s^{app} (cm^{-1})	μ_s^{corr} (cm^{-1})
30 (#1)	147.8±5.7	129.1±5.1
60 (#2)	143.4±5.1	125.2±4.5
100 (#3)	141.6±5.1	123.6±4.5
200 (#4)	148.6±4.8	129.8±4.2
5400 (#5)	115.1±2.1	100.2±1.9

Fig. 7. (a) Confocal-to-NDS fluorescence intensity ratios as a function of the imaging depth inside a ~130cm^{-1} scattering gel containing polystyrene beads of 1.53μm in diameter (g = 0.93), for the four confocal pinholes of our scanning microscope and a much larger aperture. (b) Table reporting the apparent and corrected scattering coefficient for the five apertures.

Experimental data are again well fitted by first order polynomials which are almost parallel each other. Consequently, apparent and corrected scattering coefficients, as summarized in Table 4, appear independent of the diameter of the confocal pinhole, all uncertainties included, in accordance with Monte Carlo simulations of section 3. Obtaining a higher scattering coefficient (~130cm^{-1}) than the one expected (100cm^{-1}) may be explained by experimental uncertainties on the volumes taken both from the stock solution of microbeads and from the agarose solution. The lower value of ~100cm^{-1} found with the larger aperture #5 can be accounted for Monte Carlo simulation. Indeed, a larger aperture allows scattered photons to be detected, resulting in a decrease of the apparent scattering coefficient. This effect is quite similar to the decrease observed for g values above 0.99 (see section 3).

Finally, we performed measurements on biomimetic samples consistiting of two distinct scattering gels either one above the other (superimposed) or one beside the other (juxtaposed). For the superimposed sample, a ~100cm^{-1} scattering gel containing beads of 4.52μm in diameter was extracted from a 100μm inner thickness capillary and deposited on a microscope coverslip. A ~200cm^{-1} scattering gel with 0.54μm beads was laid down on the first, and the whole sample was deposited on a microscope slide. An example of TPEF images of the two superimposed gels is given in insertion of Fig. 8(a); we can see on the left image that large polystyrene beads included in the top gel are resolved. In that case, the confocal-to-NDS fluorescence intensity ratio is expected to scale like $\exp(-\mu_{s1}^{app}.z_0)$ for $z_0 < t_1$, and like $\exp[(\mu_{s2}^{app} - \mu_{s1}^{app}).t_1] \exp(-\mu_{s2}^{app}.z_0)$ for $z_0 > t_1$. Here, μ_{s1}^{app} and μ_{s2}^{app} are the apparent scattering coefficients or the slopes of semi-log representation of the experimental fluorescence ratio as a function of the imaging depth z_0 for the first (top) and the second (bottom) gels, whereas t_1 is the thickness of the first one. The same experimental method as previously described was used, except that the imaging depth was limited to 150μm due to the high scattering coefficient of the bottom gel. The axial profile of the confocal-to-NDS fluorescence ratio reported in Fig. 8(a) well reveals a sharp break of the slope at a depth of about 80μm due to the transition from one medium to the other, with a fair exponential behavior as shown by the straight line fitting of the data in this semi-log representation. The corresponding apparent and corrected scattering coefficients are summarized in the table of Fig. 8(b). Higher values compared to those expected (100 and 200cm^{-1}) may be explained by a dehydration of the gels during the preparation stage of the assembly.

(a)

(b)

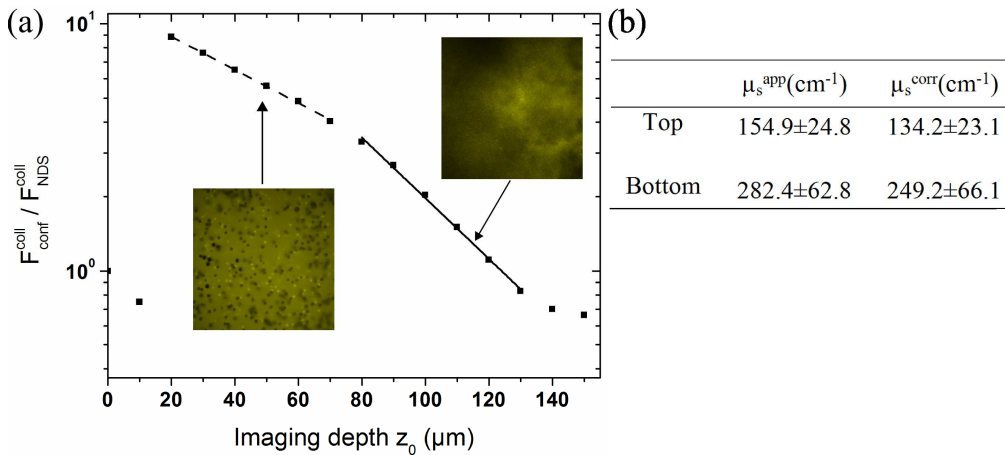|	μ_s^{app}(cm^{-1})	μ_s^{corr}(cm^{-1})
Top	154.9±24.8	134.2±23.1
Bottom	282.4±62.8	249.2±66.1

Fig. 8. (a) Intensities ratios versus imaging depth in the case of superposed gels with different scattering properties. Points represent the experimental data. Dash line is the fit of the ratio for the top gel, and continuous line for the bottom gel. Inserts are ~50 × 50μm^2 images of the gels through the NDS pathway (left: 4.52μm beads top layer imaged at 30μm depth, right: 0.54μm beads bottom layer imaged at 90μm depth). (b) Table reporting the apparent and corrected scattering coefficient of the two layers.

For the juxtaposed gels, the two samples were prepared in 500μm-width glass capillaries which were carefully broken to extract and laid down the gels side-by-side between a microscope slide and a coverslip. In order to map the scattering coefficient, z-stacks (300μm in-depth with a step size of 5μm) of 5-fold zoomed images (~50 × 50μm^2) of the area close to the interface between the gels were acquired at a definition of 2048 × 2048 pixels^2 (see Fig. 9(a)). Each image of the stack was segmented into 4096 (64 × 64) small areas. For all these areas we evaluated the apparent scattering coefficient from linear fitting of the corresponding axial profiles of the confocal-to-NDS fluorescence ratio. Areas whose fit had a R^2 value less than 0.9 were excluded (14/4096). A 64 × 64 map of the scattering coefficient (in a gray scale) obtained near the interface of the gels is reported in Fig. 9(b). Both gels are clearly

distinguished by their scattering coefficients. Furthermore an intermediate region is visible at the interface, which can be due to the fact that when the fluorescent source is deeply localized near the interface, photons can cross the two scattering media prior to be collected by the high-NA objective. The histogram corresponding to μ_s values of Fig. 9(b) exhibits two peaks around 250 and 625cm^{-1} and intermediate values reflecting the interfacial effect (cf. Fig. 9(c)). Figure 9(d) is a histogram of the R^2 value of the linear fits used to recover the apparent scattering coefficient from each block of the image, demonstrating the robustness of our method.
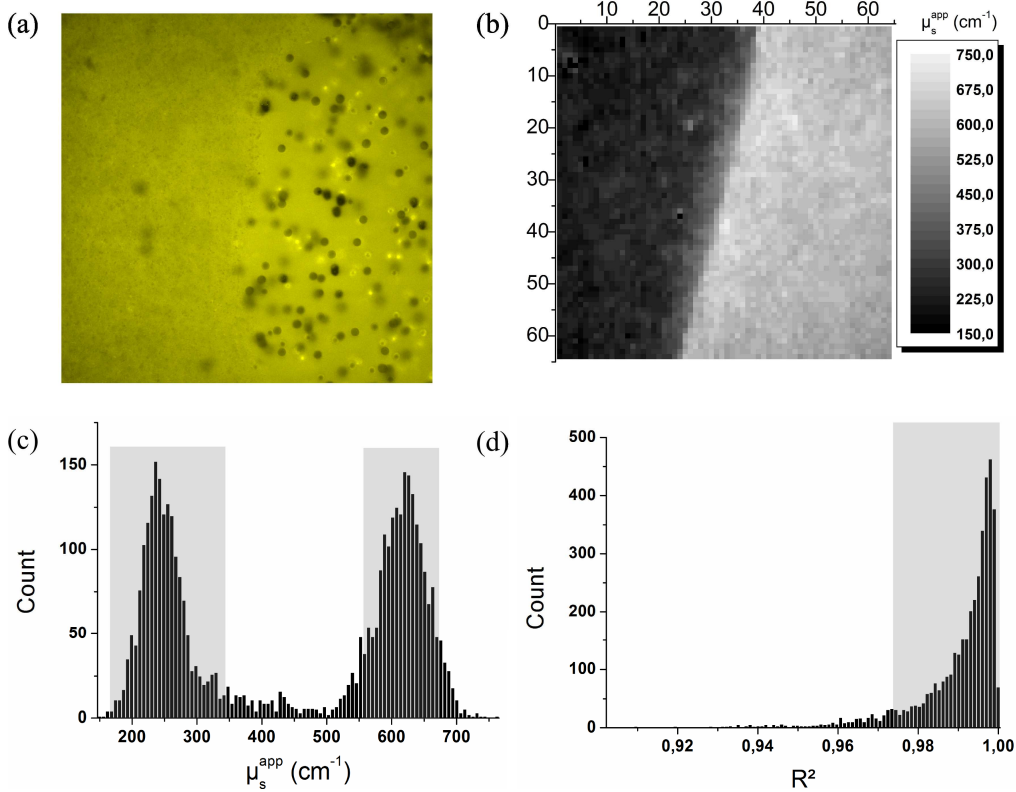

Fig. 9. Scattering coefficient imaging of two abreast gels. The left part is a 0.54μm beads gel with low μ_s, and the right part is a 4.52μm beads gel with high μ_s. (a) ~50 × 50μm^2 image of the sample through the NDS pathway, for an imaging depth of 30μm. (b) Reconstructed scattering coefficient map. (c) Histogram of μ_s^{app}. (d) Histogram of the correlation coefficient R^2. Note that 90% of the data are included within the grey areas.

7. Conclusion

We have reported an original and simple method to measure the scattering coefficient of turbid media from the intensity ratio of the fluorescence signals epi-collected through the confocal and the NDS ports of a scanning two-photon microscope. We have shown from Monte Carlo simulations that this ratio is almost independent of the absorption, of the scattering anisotropy of the medium, for g values in the range [0.8-0.99], and of the size of the confocal pinhole. Moreover our method overcomes the problem of the unknown excitation function of the microscope. By measuring the axial profile of the confocal-to-NDS fluorescence ratio, we have been able to retrieve the scattering coefficient according to a simple ballistic model of the light collection by a high-NA objective lens. The method has been validated on optical phantoms consisting of polystyrene microspheres embedded in aqueous agarose gels. Comparison of the results with a collimated transmission method

clearly demonstrated the relevance of our approach. Finally we showed that our technique enables to separate two scattering media, either juxtaposed or superimposed, from their scattering coefficients. This paves the way for a new imaging method of the scattering coefficient of biological samples that could be used for biomedical diagnosis.

Acknowledgments